Earth and Space Science

RESEARCH ARTICLE
10.1029/2019EA000893

Impacts of Humidity Adjustment Through Radar Data Assimilation Using Cloud Analysis on the Analysis and Prediction of a Squall Line in Southern China

Yujie Pan[1], **Mingjun Wang**[2], **and Ming Xue**[2,3]

[1]Collaborative Innovation Center on Forecast and Evaluation of Meteorological Disasters/Key Laboratory of Meteorological Disaster, Ministry of Education/Joint International Research Laboratory of Climate and Environment Change, Nanjing University of Information Science and Technology, Nanjing, China, [2]Key Laboratory of Mesoscale Severe Weather/Ministry of Education and School of Atmospheric Sciences, Nanjing University, Nanjing, China, [3]Center for Analysis and Prediction of Storms and School of Meteorology, University of Oklahoma, Norman, OK, USA

Key Points:
- An enhanced vertical velocity-dependent moisture adjustment scheme produces better squall line structures in both analysis and forecast
- The "overwarming" issue associated with the original scheme is linked to more latent heat release associated with higher condensation rate
- Condensation into and evaporation of cloud water dominates latent heating/cooling below the freezing level

Correspondence to:
Y. Pan and M. Wang,
yujiepan@163.com;
mjwang@nju.edu.cn

Citation:
Pan, Y., Wang, M., & Xue, M. (2020). Impacts of humidity adjustment through radar data assimilation using cloud analysis on the analysis and prediction of a squall line in southern China. *Earth and Space Science*, *7*, e2019EA000893. https://doi.org/10.1029/2019EA000893

Received 14 SEP 2019
Accepted 13 FEB 2020
Accepted article online 20 FEB 2020

Abstract This study examines the impacts of humidity adjustment in a cloud analysis system on the analysis and forecast of a squall line that occurred in southeast China on 23–24 April 2007. Radial velocity data are assimilated using the ARPS three-dimensional variational system while reflectivity data are assimilated by a cloud analysis system. Experiments with two different humidity adjustment schemes are performed, with the original and enhanced versions. Another experiment does not adjust moisture. Both schemes generally decrease the humidity in front of the convective line and increase the humidity within the convective and stratiform regions of squall line compared to no humidity adjustment, and the original scheme produces the higher humidity within precipitation regions, especially the stratiform region. Both schemes improve the forecast of squall line structure, including the leading convective line, a transition zone, and a trailing stratiform region. Among the three experiments, the enhanced scheme produces the highest precipitation forecast skill. The latent heating rates are also diagnosed to investigate the microphysical responses to the humidity adjustment. The cooling outside of the observed precipitation regions corresponding to the humidity reduction also acts to suppress spurious precipitation. Water vapor condensation into cloud water and cloud water evaporation generally dominate the latent heating/cooling below the freezing level. Compared to the enhanced scheme, the original scheme releases much more latent heat in the middle troposphere, causing more warming. This is linked to the higher cloud water condensation rate, due to the higher amount of moisture addition/adjustment by the original scheme.

1. Introduction

Doppler radar is an important tool for mesoscale and convective-scale observations that can provide the detailed structure and evolution of convective systems, such as squall lines and supercells (Biggerstaff & Houze, 1993; Broeke, 2017; French et al., 2008; Kennedy et al., 1993; Smull & Houze, 1987). Radial velocity and reflectivity are two variables obtained from Doppler radar observations. Although they are not directly linked to model prognostic variables, they still provide an opportunity to improve nowcasting and short-term forecasting via data assimilation (DA) (Hu, Xue, & Brewster, 2006; Hu, Xue, Gao, & Brewster, 2006; Jung et al., 2008; Pan et al., 2016; Tong & Xue, 2005).

To effectively use the mesoscale and convective-scale information observed by Doppler radar, many efforts had been made based on different DA methods, including the three-dimensional variational (3-DVar) and cloud analysis frameworks (Gao et al., 1999; Hu, Xue, & Brewster, 2006; Hu, Xue, Gao, & Brewster, 2006; Liu et al., 2019), the four-dimensional variational (4-DVar) framework (Sun & Crook, 1997), the ensemble Kalman filter (EnKF) (Houtekamer & Zhang, 2016; Jung et al., 2012; Tong & Xue, 2005; Xue et al., 2006), and hybrid methods (Gao & Stensrud, 2014; Kong et al., 2018; Li et al., 2012).

Because of the nonunique relationship between reflectivity and individual precipitation hydrometeors contributing to the reflectivity, the assimilation of reflectivity remains challenging. Within the 3-DVar and 4-DVar framework, reflectivity is usually assimilated by assuming warm-rain processes only (e.g., Sun & Crook, 1997; Wang, Sun, Fan, & Huang, 2013, Wang, Sun, Zhang, et al., 2013), whereas ice processes are essential for meso- and convective-scale systems (Xu et al., 1998). While it is possible to analyze mixed-phase hydrometeors from reflectivity data using 3-DVar (Gao & Stensrud, 2012; Liu et al., 2019,

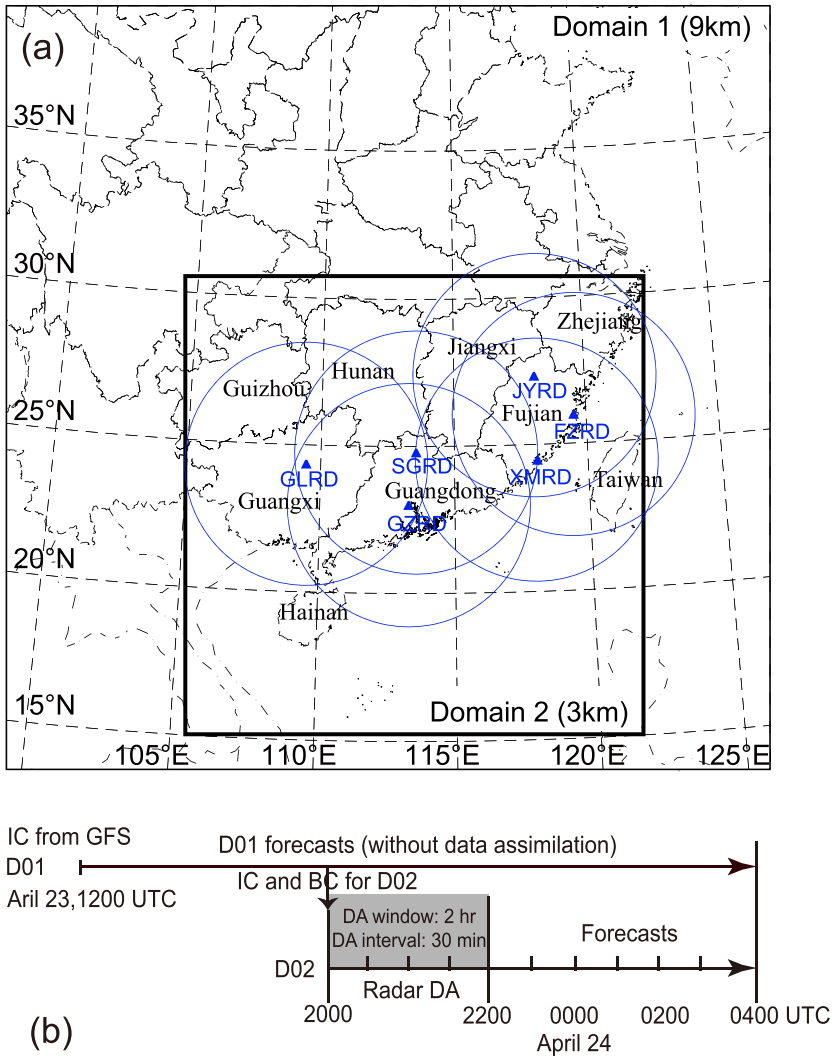

Figure 1. (a) Model domains and (b) time lines of experiments. Blue circles indicate the maximum observation ranges of the Guilin (GL), Guangzhou (GZ), Shaoguan (SG), Xiamen (XM), Fujian (FJ), and Jianyang (JY) radar. The locations of radar sites are represented by blue triangles.

2020), 3-DVar generally cannot produce by itself moisture and temperature increments from reflectivity data. With EnKF, flow-dependent background error cross covariances among reflectivity and other state variables including hydrometeor mixing ratios, temperature, and moisture are calculated from an ensemble and used by EnKF to update all state variables even with complex ice microphysics schemes (Jung et al., 2012; Tong & Xue, 2005). The EnKF method is relatively expensive, however, and has so far not used in operational convective-scale DA much.

Another approach to assimilate reflectivity data in the presence of ice microphysics is the so-called complex cloud analysis, where cloud and precipitation hydrometeors are derived from observed reflectivity based on reflectivity formulation and semiempirical rules and relations while temperature and moisture fields are adjusted based on physical considerations (Albers et al., 1996; Zhang, 1999; Hu, Xue, & Brewster, 2006). Such systems are computationally inexpensive and are often used together with 3-DVar that analyzes radial velocity and other observations and have been shown to be able to effectively initialize convective storms and alleviate the precipitation spinup problem (e.g., Albers et al., 1996; Hu & Xue, 2007; Hu, Xue, Gao, & Brewster, 2006; Kain et al., 2010; Pan & Wang, 2019; Schenkman et al., 2011).

With the complex cloud analysis, adjustment to the humidity field is a key component; without it, the reflectivity assimilation tends to lose most of its impact (Zhao & Xue, 2009; Wang, Sun, Fan, & Huang, 2013). The

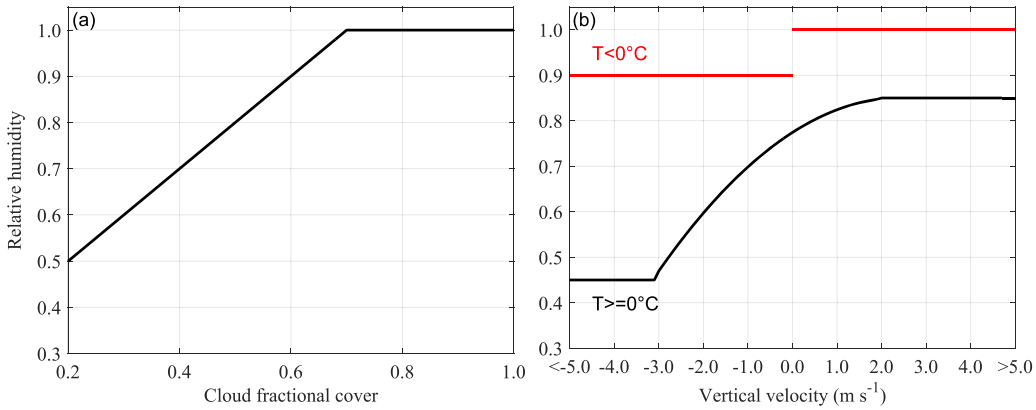

Figure 2. (a) The relationship between cloud fractional cover and relative humidity from Zhang (1999) and (b) the relationship between vertical velocity and relative humidity from Tong (2015).

inconsistent between mass and wind in the initial fields can lead to high-frequency oscillation and further degrade forecasts (Lynch & Huang, 1992). In the cloud analysis system implemented within the Advanced Regional Prediction System (ARPS) framework (Zhang, 1999), the in-cloud humidity is usually adjusted with a linear ramp from a low to high relative humidity (Hu, Xue, & Brewster, 2016; Zhang, 1999). However, adjusting in-cloud moisture repeatedly within frequently cycled reflectivity assimilation can lead to over intensification of storms, via too much heating of the midlevels (Schenkman et al., 2011). Thus, moisture adjustment (MA) is often applied only in the first DA cycle during high-frequency radar DA is performed (Pan & Wang, 2019; Pan et al., 2016; Schenkman et al., 2011). This is of course a very ad hoc solution. Proper moisture state within a cloud/storm is clearly very important for the development and evolution of the cloud/storm. Water vapor inside cloud can directly affect the formation and the phase changes of water substance associated with latent heating and/or cooling (Grabowski et al., 2019; Grabowski & Morrison, 2017). The amount of precipitable water could restrain the strength organization of squall line while the wind shear, static stability, and buoyancy energy were certain (Takemi, 2006, 2007).

Aiming to improve the MA procedure within the ARPS cloud analysis system, Tong (2015) proposed a more complex scheme with a relationship between *RH* and vertical velocity based on model simulation data and tested it using observing system simulation experiments. The application to an idealized squall line demonstrated the ability of the scheme to improve storm prediction. However, this scheme has not been tested on a real case, and the impacts of these two schemes on the analyses and forecasts of real cases need to be documented.

In this study, a squall line that occurred in southeast China on 23–24 April 2007 is used to examine the relative performance of the original MA scheme and the new scheme proposed by Tong (2015). First, the impacts of MA on analyzed fields and short-term forecasts are compared and investigated. Then, the responses of latent heating/cooling to the MA are examined by diagnosing the latent heating/cooling associated with various hydrometeor phase changes. How the MA scheme of Zhang (1999) leads to overwarming in middle troposphere is elucidated.

The rest of this paper is organized as follows. The methods and experimental design are described in section 2. The impacts of MA schemes on the analyses and short-term forecasts of the south China squall line are compared and investigated in section 3. The microphysical responses to MA are examined in section 4. Finally, the summary is provided in section 5.

2. Methods and Experimental Design

2.1. Case overview

A classic squall line occurred on 23 April 2007 in south China, with a convective line separated from a stratiform precipitation region by a transition zone. This case was used as a test case by Pan et al. (2016) to develop and test the enhanced complex cloud analysis coupled with a two-moment microphysics scheme and used

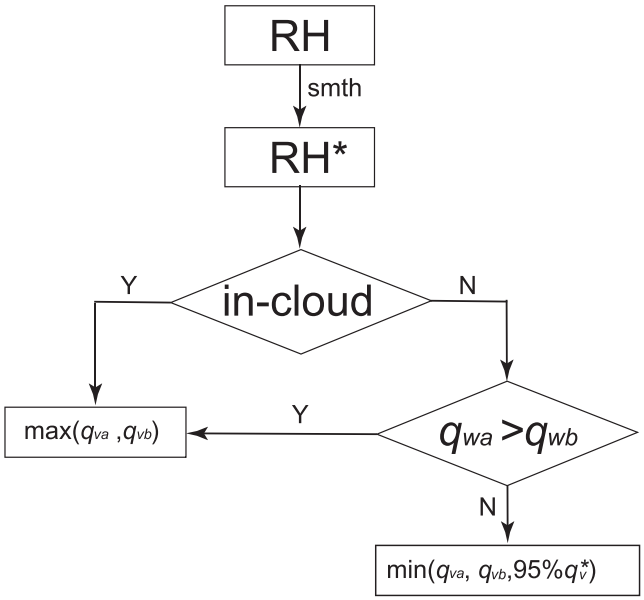

Figure 3. Flow chart of steps convert *RH* to *qv* within MAs. The q_v fields from the analysis and the background are denoted as q_{va} and q_{vb}, respectively. The q_{wa} and q_{wb} indicate analyzed total hydrometeor mass, including rain, snow, graupel, and hail, from analysis and background fields, respectively. The saturated water vapor mixing ratio from the background is denoted as q_v^*.

by Pan and Wang (2019) to evaluate the impacts of radar DA frequency with the ARPS 3-DVar and cloud analysis.

This squall line case is also used in the present study to test the impacts of MA schemes. The squall line was initiated in Guangxi Province around 2000 UTC on 23 April and moved southeast toward Guangdong Province, reaching a mature stage around 0000 UTC on 24 April. The evolution of the squall line was observed by six China New Generation 1998 Doppler radars, including those at Guangxi, Shaoguan, Guangzhou, Xiamen, Fuzhou, and Jianyang. The locations and the reflectivity ranges (460 km) are shown in Figure 1a. Radar data were manually edited to dealiase radial velocity (V_r) and remove nonprecipitation reflectivity (Z).

2.2. Model Configurations

The ARPS (Xue et al., 2000; Xue et al., 2001) is used as the prediction model in this study. The model domain is defined in Figure 1a. The outer domain at a 9-km grid spacing consists of 323 × 323 grid points, and the inner domain at a 3-km grid spacing consists of 579 × 579 grid points. The 53 vertical grid levels are stretched with an averaged 400-m grid spacing, and the grid spacing near the surface is 50 m. The 1° × 1° NCEP Final Operational Global Analysis data are used as the initial and boundary conditions for the outer domain. The main physics parameters for the forecasts are the Milbrandt-Yau double-moment microphysical parameterization scheme (Milbrandt & Yau, 2005), four-order horizontal and vertical advection, fourth-order computational mixing, 1.5-order turbulence kinetic energy-based subgrid-scale boundary layer turbulent mixing parameter scheme (Sun & Chang, 1986), a two-layer land surface model (Noilhan & Planton, 1989), and Goddard Space Flight Center long- and short-wave radiation parameterization (Chou, 1990).

2.3. Data Assimilation Configurations

Sixteen-hour forecasts initiated from 1200 UTC 23 April are carried out without DA for the outer domain. The forecasts during 2000 UTC 23 and 0400 UTC 24 are interpolated into the inner domain as the initial and boundary conditions, respectively. V_r and Z data from six radars are assimilated every 30 min from 2000 UTC to 2200 UTC via ARPS 3-DVar and cloud analysis. Based on the final analyses, 6-hr forecasts are conducted until 0400 UTC 24 April.

V_r data are assimilated via ARPS 3-DVar with a weak anelastic mass continuity constraint (Gao et al., 2004) every 30 min. After the V_r assimilation, Z data are assimilated using the ARPS cloud analysis system, extended by Pan et al. (2016) to support both mixing ratios and total number concentrations of hydrometeros associated with the Milbrandt-Yau double-moment microphysics scheme (Milbrandt & Yau, 2005). In the system, the hydrometeor species are first diagnosed according to the observed reflectivity and the background temperature, and then the mixing ratios and total concentrations of rainwater, snow, hail, and graupel are retrieved based on the reflectivity equations. More details can be found in Pan et al. (2016). Next, the in-cloud temperature is adjusted by assuming a modified moist adiabatic ascent accounting for entrainment (Hu, Xue, & Brewster, 2016) in correspondence with analyzed hydrometeor distributions. The MA scheme adjusts the relative humidity (*RH*) instead of the water vapor mixing ratio (q_v) to avoid supersaturation. q_v is then calculated according to the adjusted *RH* and the temperature.

Table 1
List of Experiments in This Study

Experiment name	Humidity adjustment method
NMA	–
ZMA	Zhang (1999)
TMA	Tong (2015)

2.4. Moisture Adjustment Schemes

Within the cloud analysis system, the moisture is adjusted via empirical methods owing to the lack of direct observation of humidity. Both MA schemes are applied to the in-cloud region where the cloud fractional cover (CFC) is greater than a low threshold value of 0.2 in this study. More details about the method determining the cloud cover can be referred to Zhang (1999). Two MA schemes are briefly introduced below.

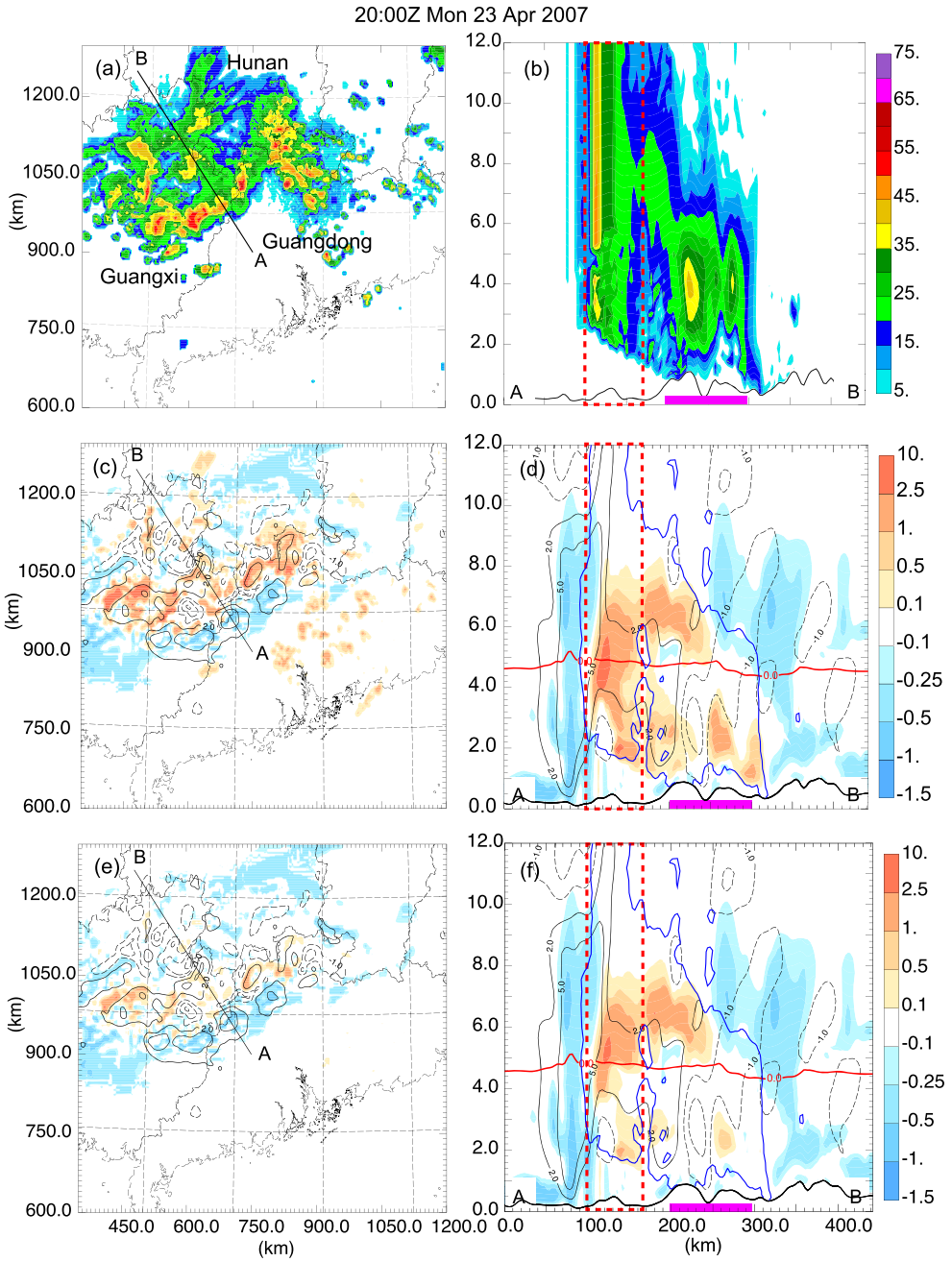

Figure 4. (a) Observed composite radar reflectivity and (b) cross section of mosaic reflectivity (shading, units: dBZ) along A–B of the squall line at 2000 UTC, 23 April 2007. The increments of water vapor mixing ratio before and after DA (shading in c–f; units: g kg^{-1}) and vertical velocity (contours in c–f; units: m s^{-1}) at 3 km from experiments ZMA (c) and TMA (e) at 2000 UTC, 23 April 2007, and their cross sections along A–B. Updrafts are in solid lines, and downdrafts are in dashed lines; the red line indicates the freezing level, and the blue line in (d) and (f) indicates 5 dBZ of mosaic reflectivity. The red dashed rectangle indicates the convective region, and the purple line marks the stratiform region.

The original MA scheme was initially proposed and applied to cloud analysis by Zhang (1999). This MA scheme modifies the in-cloud *RH* for CFC between 0.2 and 0.7 using a linear ramp from 50% to 100% (Figure 2a).

Recently, a more complex and realistic enhanced MA scheme was proposed by Tong (2015) to improve the analyses and forecasts via reflectivity assimilation. Based on extensive observing system simulation

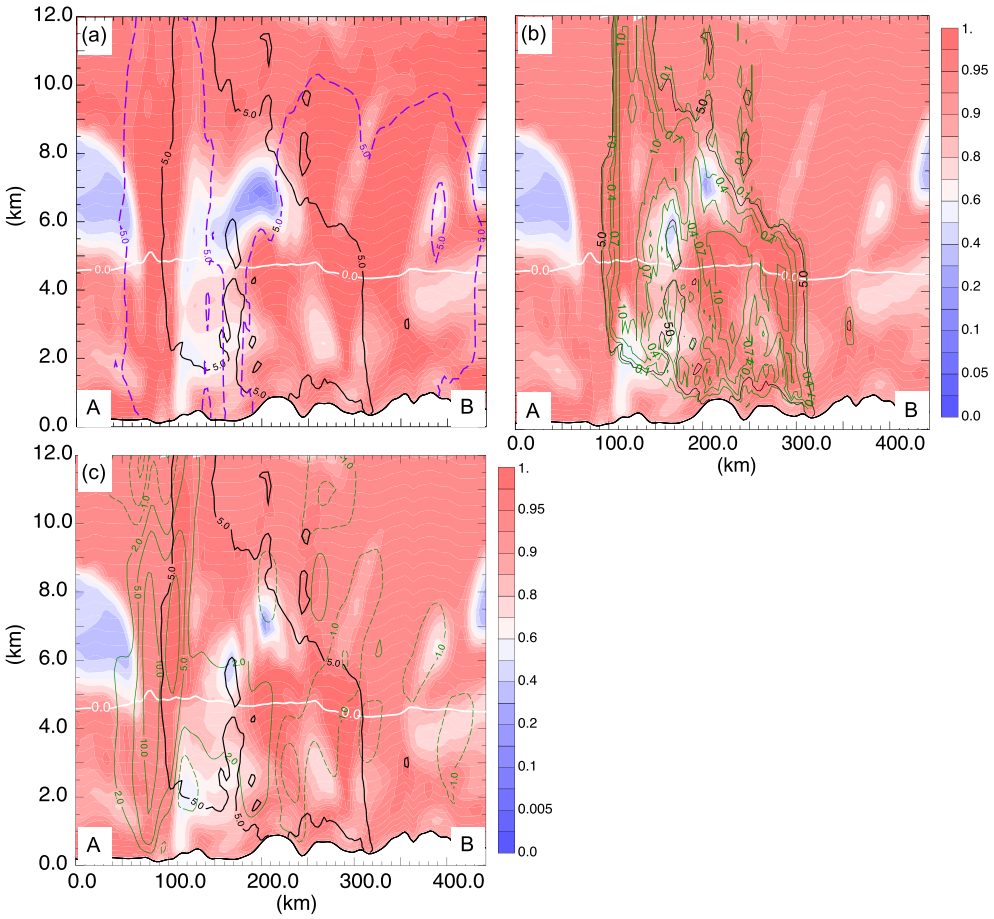

Figure 5. Vertical cross sections of analyzed fields along A–B in Figure 3a showing relative humidity (shading) with freezing line (units: °C, white solid line) and observed mosaic reflectivity (5 dBZ, solid black line) at 2000 UTC, 23 April 2007 for experiments (a) NMA, (b) ZMA, and (c) TMA. The mosaic reflectivity from background at 5 dBZ (dashed purple line) is overlaid in (a), cloud fractional cover (green solid line) is overlaid in (b), and vertical velocity (green solid line) is in (c) (units: m s^{-1}, green lines).

experiments, the relationship between *RH* and vertical velocity (w) was established. *RH*-w relationships were retrieved above and below freezing level separately considering the *RH* values show significantly different features in those two regions. The statistical results suggested that the negative w outlines most unsaturated area above the freezing level. Under the freezing level, the *RH* distribution was highly scattered. Several regression relationships between *RH* and w were obtained via different regression methods. Sensitivity experiments employed different retrieved relationships and constant *RH* for $w < 0$ (80%–90% with 1% interval), $w > 2$ ms^{-1} (85%–99% with 1% interval), and $w < -3$ ms^{-1} (40%–60% with 1% interval) were further tested. The RH values with the minimum square root error were chosen for the moisture adjustment. The in-cloud humidity is adjusted as follows:

$$\begin{cases} T<0oC \begin{cases} w\geq 0\ ms^{-1}, & RH = 100\% \\ w<0\ ms^{-1}, & RH = 90\% \end{cases} \\ T\geq 0oC \begin{cases} w\geq 2\ ms^{-1}, & RH = 85\% \\ -3\ ms^{-1}\leq w<2\ ms^{-1}, & RH = -1.29\,w^2 + 6.28\,w + 77.43 \\ w<-3\ ms^{-1}, & RH = 45\% \end{cases} \end{cases} \quad (1)$$

In this scheme, the in-cloud region is separated into two layers, above and below the freezing level. Above the freezing level ($T < 0^oC$), the air is almost saturated ($RH > 90\%$). Below the freezing level ($T \geq 0^oC$),

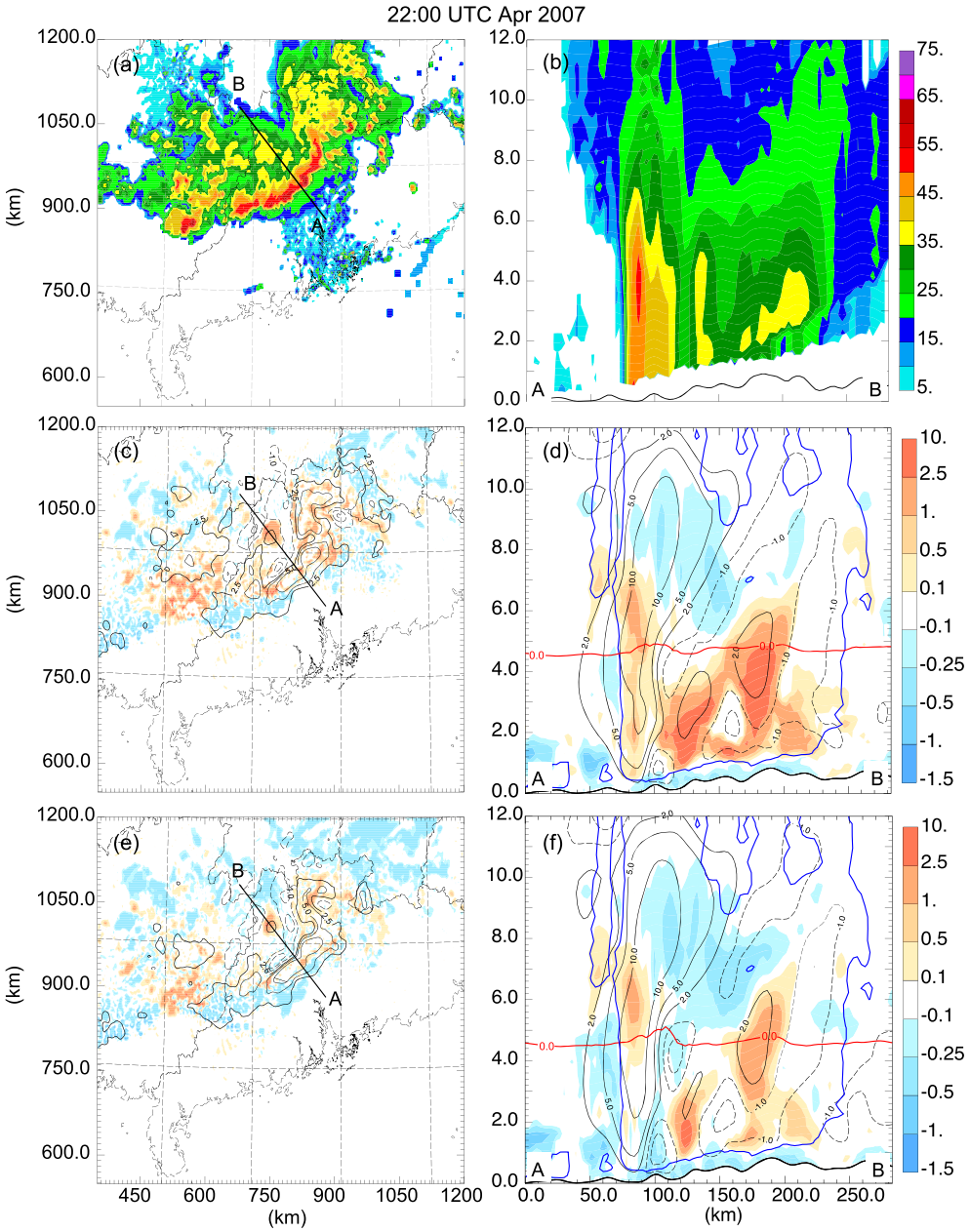

Figure 6. The same as Figure 3 but for 2200 UTC, 23 April 2007.

the relationship is obtained through a second-order regression of *w* and *RH*. As shown in Figure 2b, the *RH* is 45% when *w* is less than −3.0, and 85% when *w* is greater than 2.0 m s^{-1}. When w is between −3.0 and 2.0 m s^{-1}, the *RH* is calculated according to the second-order regression relationship.

Although these two MA schemes modify *RH* based on independent relationships, similarities and differences between these two schemes can be expected. Below the freezing level, the original scheme tends to add more water vapor than the enhanced scheme when CFC is larger than 0.6 or *w* is less than −3 m s^{-1}. Above the freezing level, these two schemes tend to produce similar *RH* when CFC is larger than 0.6. Since most of CFC values within the precipitation regions are over 0.6, the original scheme tends to produce more (similar) water vapor compared to the enhanced scheme below (above) the freezing level.

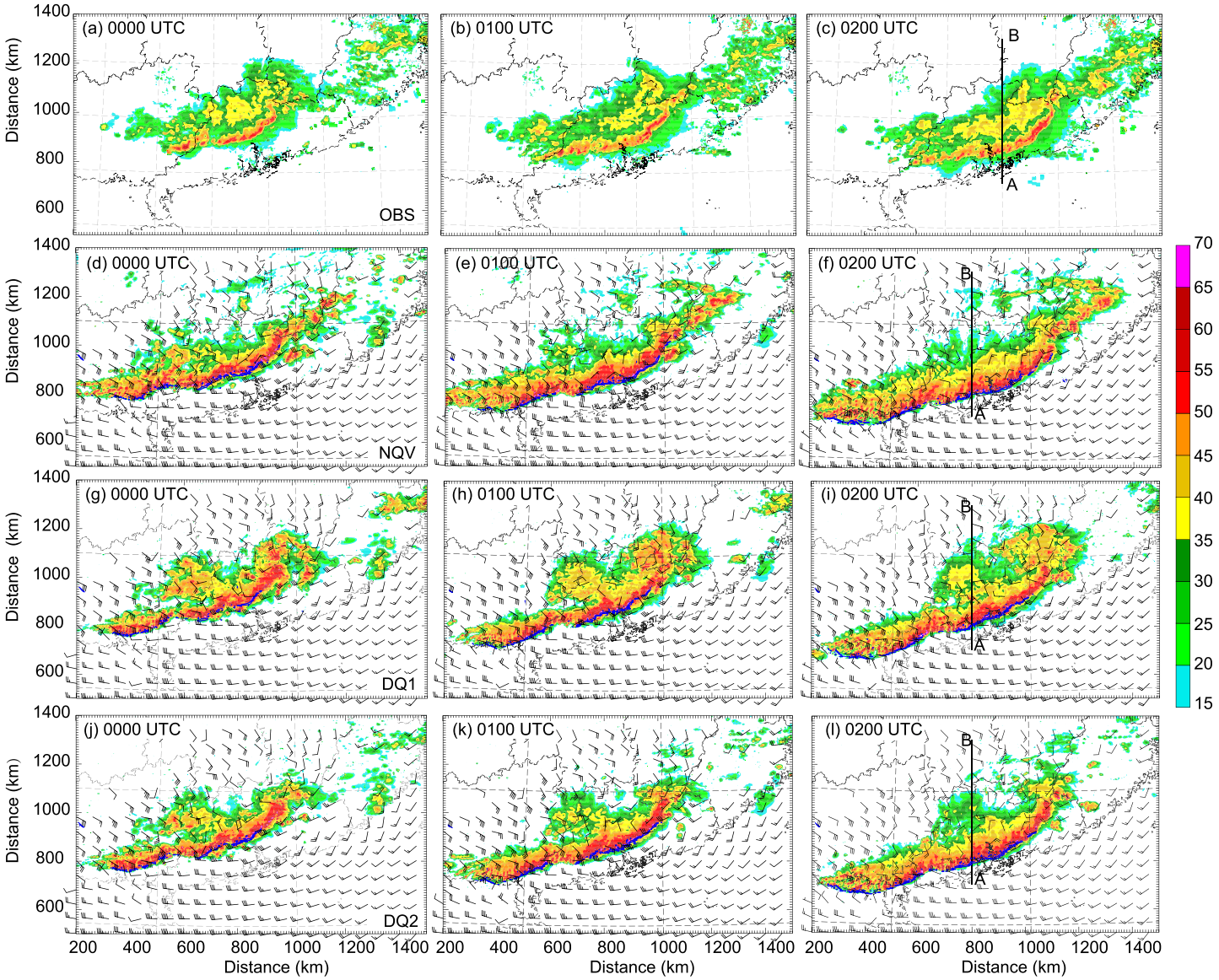

Figure 7. The observed (a–c) and predicted composite reflectivity (shading, units: dBZ) from experiments NMA (d–f), ZMA (g–i), and TMA (j–l) at 0000, 0100, and 0200 UTC, respectively. The wind bars indicate storm relative wind (units: m s^{-1}) at 500-m AGL. Blue lines are vertical velocity in 1.0 m s^{-1}. The solid line A–B indicates the slide position for Figures 10–12.

After MA, the *RH* is set to the larger one of the adjusted value and the background value. Then, as shown in Figure 3, a three-dimensional smooth operator is applied to *RH* twice to mitigate the sharp gradient in cloud region first. Then, the in-cloud q_v is set to the maximum of diagnosed q_v from analyzed field (q_{va}) calculated by adjusted *RH* and q_v from the background (q_{vb}). Outside the cloud, if the analyzed total hydrometeor mass (q_{wa}, including rain, snow, graupel, and hail) is less than the background (q_{wb}), then q_v is set to the minimum among q_{va} and q_{vb}, and 95% of the saturated water vapor mixing ratio (q_v^*), which is a function of pressure and temperature. Otherwise, q_v is set to the larger one of q_{va} and q_{vb}.

To better distinguish these two methods, we designate the method proposed by Zhang (1999) as the "Zhang scheme" and the one proposed by Tong (2015) as the "Tong scheme." We conducted three experiments (Table 1) to investigate the impacts of the enhanced scheme on analyses and subsequent forecasts, also shed some light on reasons for the unrealistic heating at the low to middle levels of the troposphere, observed when using the Zhang scheme. Experiment NMA, without q_v adjustment, is conducted as a benchmark.

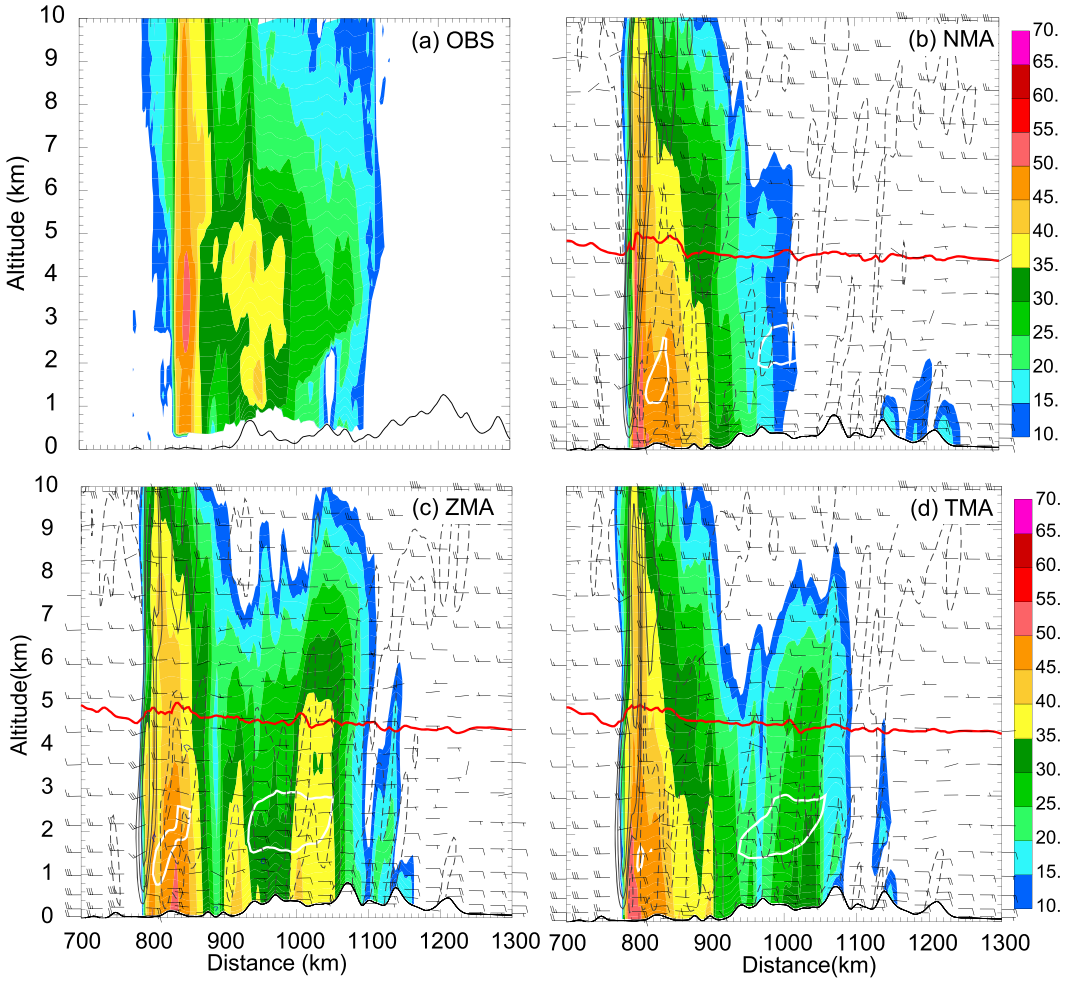

Figure 8. Cross sections of reflectivity (shading) from (a) observations, (b) NMA, (c) ZMA, and (d) TMA along A–B at 0200 UTC in Figure 5. The red line is the freezing level, and the white lines denote the area where horizontal velocities are greater than 18 m s^{-1} below 3.0 km; solid gray lines indicate updrafts at 0.2, 1.0, 2.0, and 4.0 m s^{-1}, and while gray dashed lines indicate downdrafts at −0.1, 0.4, −1.0, and −3.0 m s^{-1}.

Experiments ZMA and TMA employ the Zhang and Tong MA schemes, respectively. The MA schemes are applied to every DA cycle in our study.

3. Impacts on the Analyses and Forecasts

3.1. Impacts on the Analyses

To isolate the impacts of moisture adjustment, the analyses at the first DA cycle from the three experiments are firstly compared. Because the background at the first cycle is the same for all experiments, only the analyzed q_v fields differ from each other due to the moisture adjustment. The q_v increments (the q_v field from ZMA/TMA minus that from the background) at the first cycle are calculated and plotted along with the observed reflectivity (Figure 4). As shown in Figure 4a, the squall line was located at the junction of Guangdong, Guangxi, and Hunan Provinces at 2000 UTC on 23 April. The convective region is consisted of isolated convection, and a wide stratiform region is to the northwest behind the convective line. The vertical section across A–B (Figure 4b) also shows the same characteristics. For both ZMA and TMA, q_v is reduced by 0.1–0.25 g kg^{-1} at the leading edge of the squall line (Figures 4c and 4e). Within the precipitation area (the precipitation region is defined as the area where reflectivity is greater than 5.0 dBZ), both MA schemes generally increase the humidity at the 3-km altitude, whereas the increments from ZMA are higher than those from TMA. The vertical cross sections along A–B clearly show that the water vapor within the

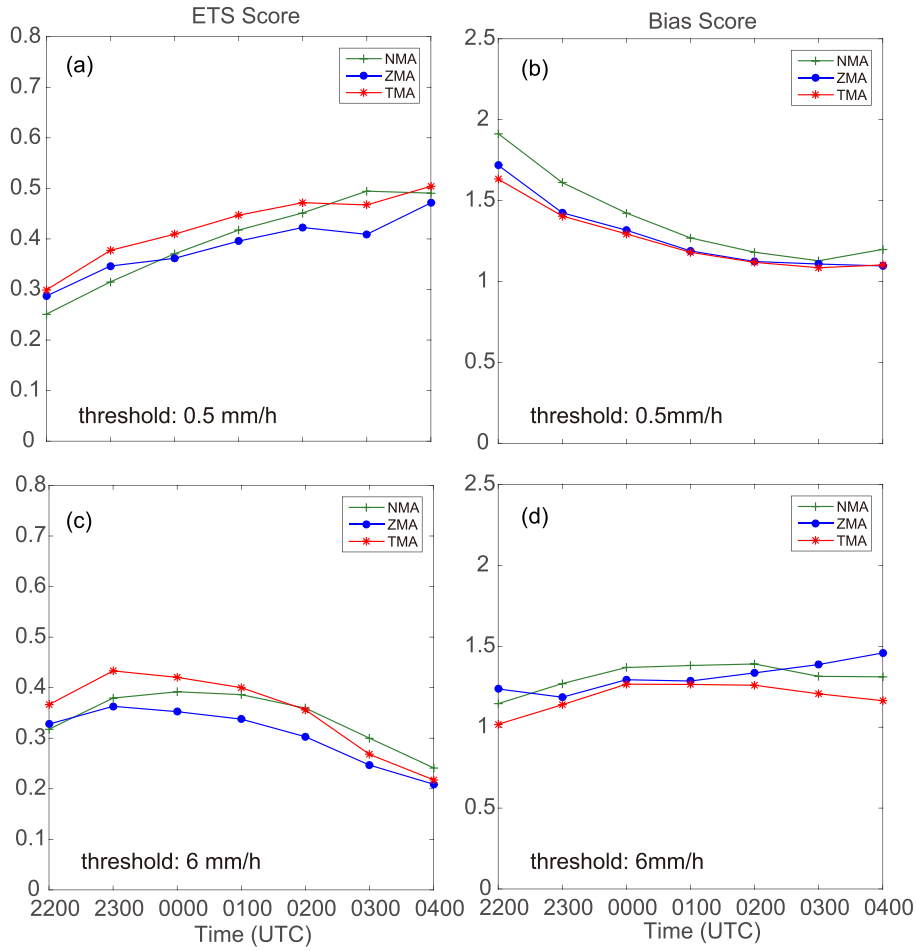

Figure 9. Equitable threat and bias scores verified against hourly rainfall at thresholds of 0.5 mm hr^{-1} (a, b) and 6 mm hr^{-1} (c, d) for experiments NMA, ZMA, and ZMA from 2200 UTC 23 April to 0400 UTC 24 April.

convective region (dashed rectangles in Figures 4d and 4f) is substantially increased with MAs, with maximum q_v increments over 2.5 g kg^{-1}. The positive increments from TMA are stronger than those in ZMA from 2- to 5-km height in the squall line. Due to vertical velocities over 2 m s^{-1} in this region (Figure 4f), Tong scheme sets the *RH* to 85%, leading to the negative increments in TMA. The q_v increments from ZMA below the freezing level within the stratiform region are higher than those in TMA.

The cross sections of *RH* are given in Figure 5 to examine the different behaviors of two MA schemes. *RH* from NMA is the same as the background since *RH* is not adjusted. As shown in Figure 5a, the location of the squall line in the background is about 50 km ahead of the observations and thus ahead of the analyses from ZMA and TMA. After DA, the *RH* is 100% and none hydrometeors existed in analyzed fields in front of the convective line. Following MA schemes, q_v is set to 95% of the saturated water vapor mixing ratio in both ZMA and TMA, corresponding to the negative increments ahead of the convective region (Figures 4c–4f). The negative increments behind the whole system are caused by the same mechanism. Therefore, MA schemes can somehow suppress the spurious precipitation through reducing the q_v, besides of the direct hydrometeor mixing ratio modification by the cloud analysis. Overall, the MA schemes increase the water vapor in the precipitation area. Zhang scheme adds more water vapor below the freezing level, consistent with different adjustment formula (Figure 2).

To examine the overall effects of MA schemes after 2-hr DA cycles, squall line structures along with q_v differences (the q_v field from ZMA/TMA minus that from NMA) at 2200 UTC are plotted in Figure 6. The squall line has a classic structure consisting of a leading convective line with reflectivity greater than 50 dBZ and a

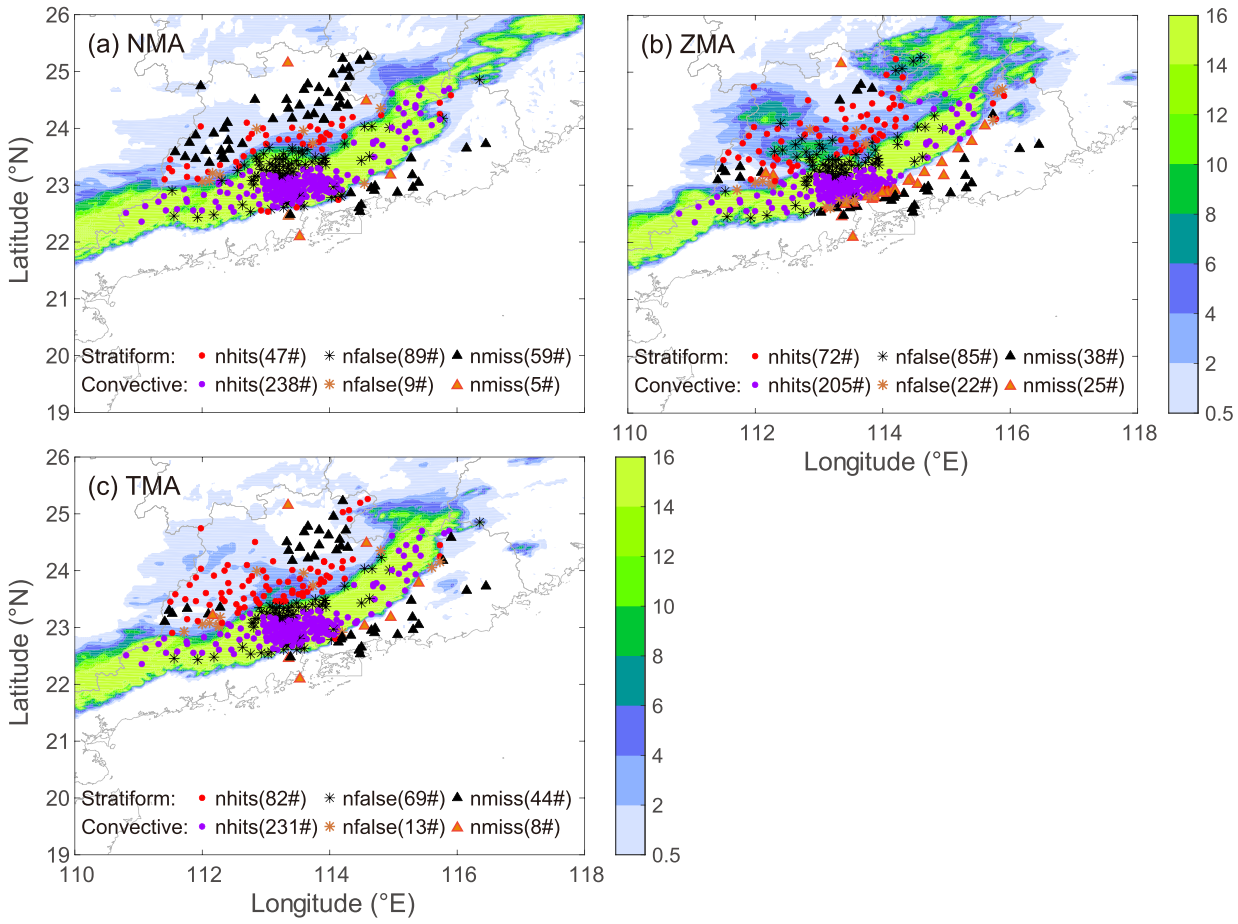

Figure 10. Predicted (shading) 1-hr accumulated rainfall along with locations of hits, false alarms, and misses for predicted 1-hr rainfall at 0100 UTC on 24 April 2007.

trailing stratiform region with reflectivity of 20–45 dBZ (Figure 6a). The vertical cross section along A–B (Figure 6b) also exhibits a tall and intense convective region with a reflectivity core at around 4-km height, followed by a stratiform region with a transition zone in the middle.

At the last cycle, ZMA and TMA have similar horizontal distributions of q_v differences. Negative values are noticed ahead of the convective line for both ZMA and TMA (Figures 6c and 6e), which is the same as the first cycle. Both schemes increase q_v in the stratiform region at the 3-km level shown, while ZMA added more q_v than TMA in terms of the higher magnitude and the larger coverage of positive differences. Vertical cross sections along A–B in ZMA (Figure 6d) and TMA (Figure 6f) also show similar structures of q_v differences. Negative values are generally distributed in front of the convective region and above the freezing level in the transition zone and stratiform region. Positive q_v adjustment is collocated with the core updrafts in the convective and stratiform regions, suggesting that both schemes increase moisture in the updraft regions. In general, ZMA and TMA have similar distributions of q_v differences, while ZMA adds more water vapor than TMA does at the first cycle. Moreover, the magnitude and coverage of positive differences from ZMA are significant enlarged, while TMA has the lower minimum and larger coverage of the negative difference after cycles.

3.2. Impacts on Short-Term Forecasts

The observed squall line exhibited a classic structure with a convective line, trailing stratiform region, and a transition zone (Figures 7a–7c). Compared to observations, all simulations accurately predict the southeastward motion but have longer and wider convective lines. With MA, the stratiform region is more accurately predicted in ZMA and TMA, and part of the transition zone is also reproduced by ZMA and TMA. In

Table 2
List of Microphysical Processes Examined Relative to Latent Heating and Cooling

Heating	Cooling
Cloud Condensation	Cloud evaporation
Rain Condensation	Rain evaporation
Ice Deposition	Ice sublimation
Snow Deposition	Snow sublimation
Graupel Deposition	Graupel sublimation
Hail Deposition	Hail sublimation
Cloud to Ice Freezing	Ice melting
Cloud to Ice Collection	Snow melting
Cloud to Snow Collection	Graupel melting
Cloud to Graupel Collection	Hail melting
Cloud to Hail Collection	
Rain to Hail Collection	
Rain to Ice Collection	
Rain to Snow Collection	
Rain to Graupel Collection	
Rain to Hail Collection	

comparison, there are no obvious stratiform and transition features in NMA at 0100 and 0200 UTC. In general, the moisture adjustment improves the short-term forecasts in terms of the squall line structure. The vertical cross sections along A–B in Figure 7 at 0200 UTC are plotted in Figure 8. Because the length of the squall line differs between the forecast and observations, we plot the cross sections through the middle of the respective squall line. As shown in Figure 7, NMA misses the stratiform region entirely while ZMA and TMA capture both the stratiform region and weak reflectivity transition zone. The stratiform region in ZMA is stronger, corresponding to the higher q_v below the freezing level within the stratiform region.

To objectively evaluate the impacts of MA on short-term forecasts, equitable threat scores (ETSs) and bias scores (Schaefer, 1990) are verified against the observed hourly accumulated rainfall from rain gauge measurements at thresholds of 0.5 and 6.0 mm hr^{-1} (Figure 9). For the 0.5 mm hr^{-1} threshold, ZMA outperforms NMA only in the first hour of forecast. Afterward, its ETSs are generally lower than those of NMA, indicating that the original MA scheme has deficiency that limits its positive impact beyond a very short period of forecast. Using the enhanced MA scheme in TMA, the ETSs are higher than those of NMA during the first 4 hr of forecast and those of ZMA for the entire 6-hr forecast at both 0.5 and 6 mm hr^{-1} thresholds. In addition, TMA has the lowest precipitation biases among all three experiments and NMA has the highest positive biases. Overall, TMA has the highest precipitation forecast skill, suggesting that the Tong scheme may have produced the most accurate moisture analysis.

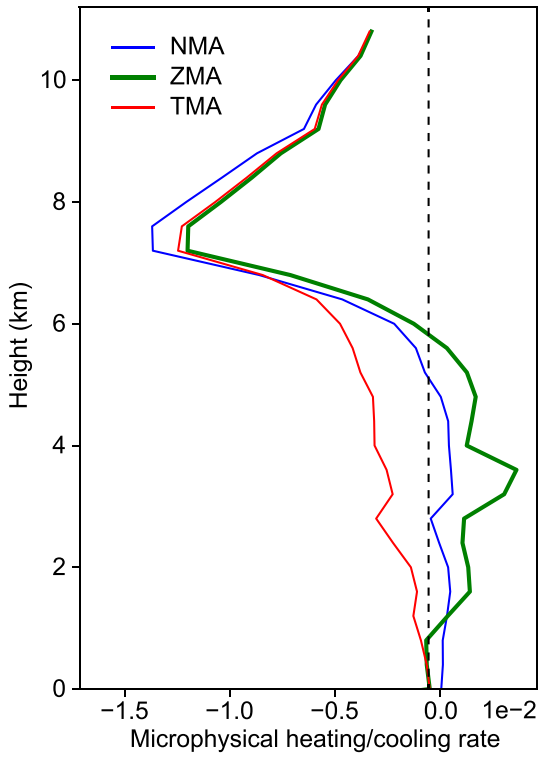

Figure 11. The averaged microphysical heating/cooling rate (units: K s^{-1}) profile from 2000 to 2030 UTC at 10-min intervals.

To see how forecast rainfall affects the forecast skill scores, the predicted hourly rainfall is directly compared against the observations at individual observation sites (Figure 10). We define stratiform rainfall as hourly rainfall rates greater than 0.5 mm hr^{-1} but less than 6 mm hr^{-1}, and convective rainfall as hourly rainfall rates greater than 6 mm hr^{-1}. If both forecast and observation are identified as stratiform rainfall, that point is flagged as a "hit." If the forecast is stratiform but the observation is not, it is a "false alarm." If the forecast is not stratiform but the observation is, then it is a "miss." The same rule is applied to convective rainfall. The numbers of hits, false alarms, and misses for stratiform and convective rainfall are counted and plotted in Figure 10, together with the locations. Without MA in NMA, the overall rainfall area is the smallest, especially for stratiform rainfall. ZMA has the narrowest convective precipitation band and has two intense precipitation centers around 114–116°E, 24–26°N and 111–114°E, 23–25°N outside the convective band. The false alarm points of stratiform rainfall are located mainly behind the middle part of the convective rain band; there are more false alarms for ZMA than for TMA and NMA. The superior stratiform forecasts in ZMA and TMA (Figure 8) lead to more stratiform rainfall hits and fewer misses. The stratiform rainfall in ZMA is more intense than that in TMA, which can be attributed to the higher humidity in the stratiform region in ZMA (Figures 4 and 6). As a result, the stratiform rainfall hits in ZMA are fewer than those in TMA. A northward shift of the right half of the convective rain band in ZMA compared to NMA and TMA results in the fewest hits for convective rainfall. NMA and TMA have comparable convective rainfall prediction accuracy. Overall, TMA has the highest forecast skill among all experiments according to the horizontal rainfall distributions, consistent with the summary ETS scores seen earlier.

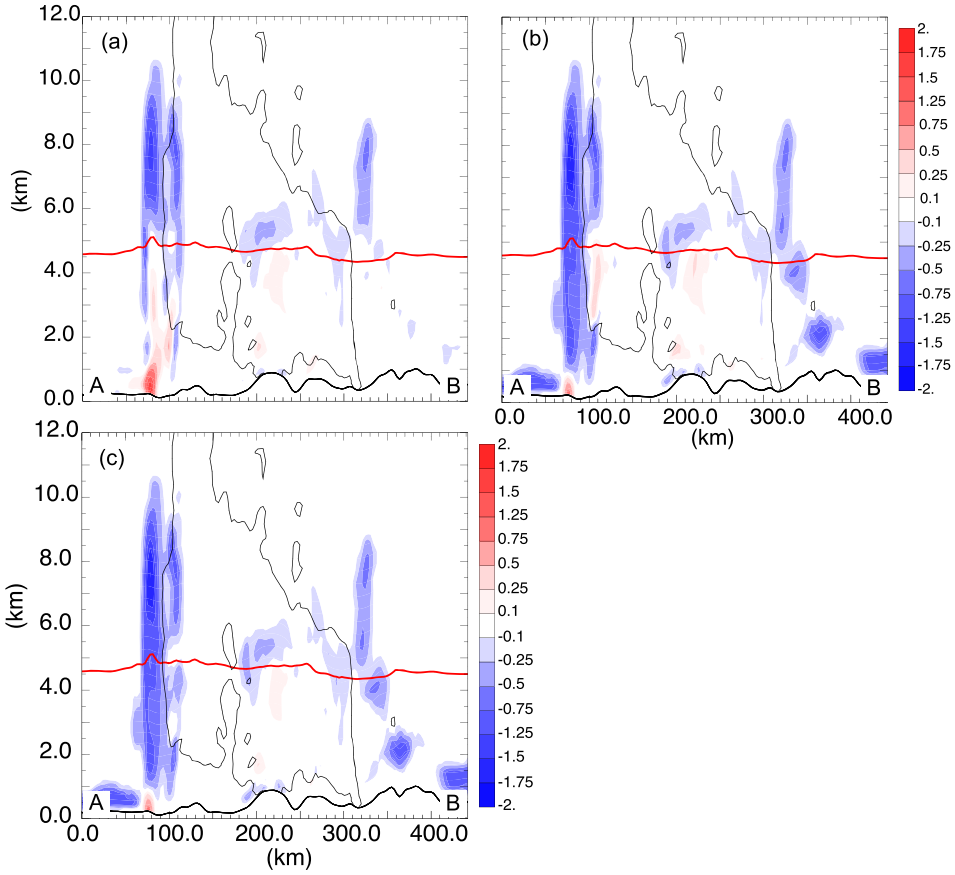

Figure 12. The cross sections of latent heat (shading, units: K s^{-1}) from (a) NMA, (b) ZMA, and (c) TMA along A–B in Figure 3a at 2000 UTC, 23 April 2007. The red line indicates the freezing level, and the solid black line is 5 dBZ of mosaic reflectivity.

According to the predicted squall line structures, experiments with MA schemes outperform that without MA, suggesting the benefit of MA for improving squall line forecasts, especially in improving the predicted squall line structure. The original MA scheme produced more moisture inside the cloud, leading to wider and stronger precipitation. With the enhanced MA scheme, TMA produces better rainfall predictions, especially for the stratiform rainfall. Both objective and subjective verifications indicate that the enhanced MA scheme produces the best structure and rainfall forecasts of the squall line in our test case, suggesting that its final analysis is the best among the three experiments.

4. Microphysical Responses to Humidity Adjustment

The humidity could directly affect microphysical processes related to latent heat release/absorption, including evaporation and condensation of cloud and rain, sublimation, melting and deposition of each ice category, and collection of cloud and rain by each ice category (processes are listed in detail in Table 2). To understand the microphysical responses to the MA, the instantaneous mixing ratio change rates of those microphysical processes are dumped for subsequent 30-min forecasts with a 10-min interval. The cooling and heating rate are calculated following $\Delta T = (L_{v,f,s}/C_p)\Delta q$, where Δq is the hydrometeors mixing ratio change rate due to each microphysical process at each grid cell; $L_{v,f,s}$ is the appropriate latent heat of evaporation (L_v), fusion (L_f), and sublimation (L_s); and C_p is the specific heat at constant pressure. In this section, the responses of the microphysical processes to the humidity adjustment are examined.

The vertical profiles of the total heating/cooling rates are averaged over the precipitation regions for all experiments (Figure 11) from 2000 to 2030 UTC with a 10-min interval. Above 6.5 km, all experiments

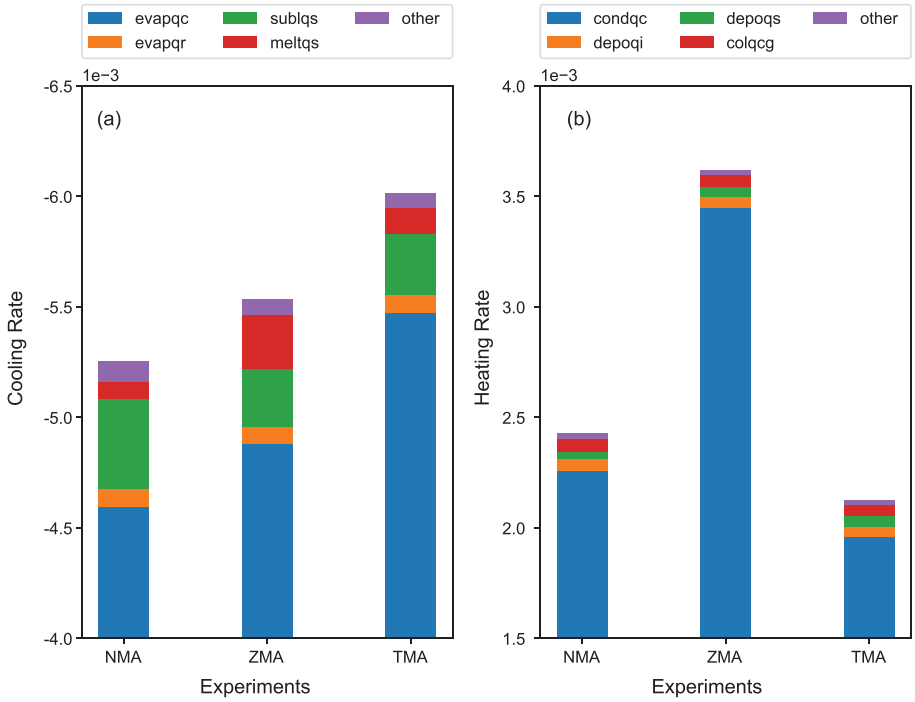

Figure 13. The major averaged temperature change rate (units: K s^{-1}) from (a) cooling and (b) heating microphysical processes in the precipitation region (defined as all grids where reflectivity is greater than 5 dBZ) from 2000 to 2030 UTC at 10-min intervals. (evapqc: cloud evaporation: evapqr: rain evaporation; sublqs: sublimation of snow; meltqs: snow melting; condqc: cloud condensation; depoqs: snow deposition; depoqi: ice deposition; and colqcg: cloud to graupel collection)

show similar cooling rates. Below 6-km height, TMA exhibits overall cooling rates whereas NMA and ZMA shows overall heating rates. It is hard to determine which profile is more accurate without direct observations. In a sense, the fact that TMA has the best rainfall forecasts suggested that the latent heat release in TMA might be more reasonable. Compared to TMA, ZMA is characterized by heating in the low-middle troposphere that might lead to relative worse forecasts.

We notice that latent heat release is the most significant in the next few integration steps after DA, due to the model adjustment to reestablish the balances. The latent heat release right after 2000 UTC contributes the most to the averaged latent heat profile (Figure 11). A cross section of latent heating/cooling at 2000 UTC from all experiments is plotted in Figure 12 to provide more details about vertical variations of latent heat release. Consistent with the q_v reduction made by MA schemes (Figure 4), ZMA and TMA show cooling in front of the convective line (Figures 12b and 12c). In comparison, NMA still shows heating below the freezing level probably related to the active condensation in this region with the saturated air and strong updraft. Within the precipitation regions (recall that reflectivity is over 5 dBZ), all experiments show cooling rates above the freezing level with similar distributions and magnitudes, which is consistent with the vertical profiles (Figure 11). The heating mainly occurs under the freezing level for all experiments (Figure 12). The major differences among three experiments are located at the leading edge and within the stratiform region. At the leading edge, ZMA and TMA produce heating and cooling rates, respectively, while the heating or cooling rates of NMA are in between ZMA and TMA. It is consistent with the q_v increments and *RH*s from ZMA and TMA (Figures 4 and 5). By averaging heating rates in precipitation region, TMA generally shows cooling rates below the freezing level (Figure 11).

To see how the microphysical processes respond to the humidity adjustment, we compare the latent heating/cooling rates of all related processes (Table 2) and examine the most important ones. The latent heating/cooling rates associated with those processes are averaged within the precipitation region and plotted in Figure 13. The evaporations of cloud water and rainwater and the sublimation and melting of snow are the main sources of cooling while the condensation of cloud water, deposition of snow and ice, and collection of cloud droplets by graupel are the main sources of heating, with the

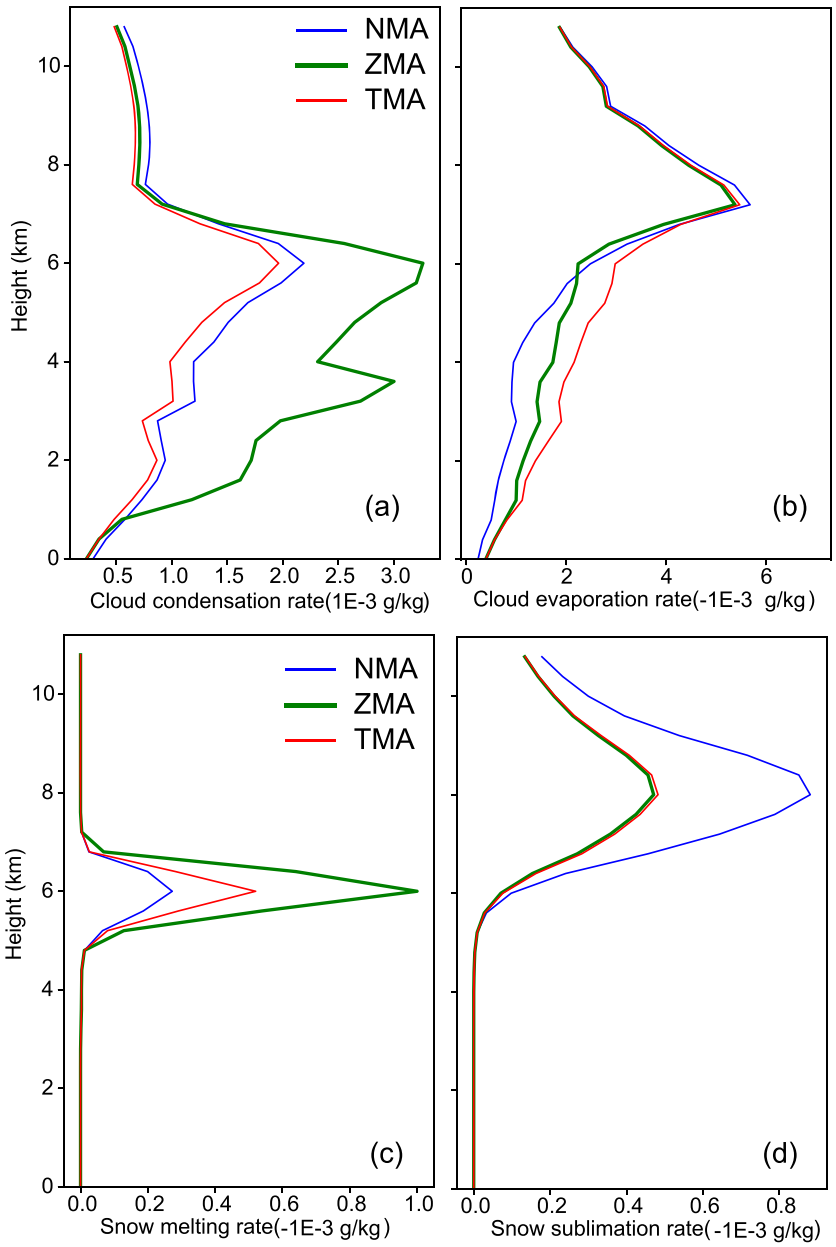

Figure 14. The profiles of transfer rates from major microphysical processes of (a) cloud condensation, (b) cloud evaporation, (c) snow melting, and (d) snow sublimation. Cloud condensation is associated with latent heating; cloud evaporation, snow melting, and snow sublimation are associated with latent cooling.

condensation/evaporation of cloud water being the largest, not surprisingly. Without moisture adjustment, NMA produces the least cooling by the evaporation of cloud water and melting of snow and the largest cooling by the sublimation of snow (Figure 13a). Cooling caused by evaporation of cloud water in TMA is most significant (Figure 13a), which may have contributed to the overall cooling below 6 km for TMA (Figure 11). The heating rate of cloud water condensation is generally an order of magnitude higher than the other processes (Figure 13b), indicating that the condensation into cloud water dominated the latent heat release. The heating rate of condensation into cloud water in ZMA, which is the highest among all experiments, likely induced the middle-low level warming (Figure 13).

To better understand the activation height of each microphysical process, the averaged profiles of the major sources of cooling and heating and cross sections of major microphysical sources along A–B in

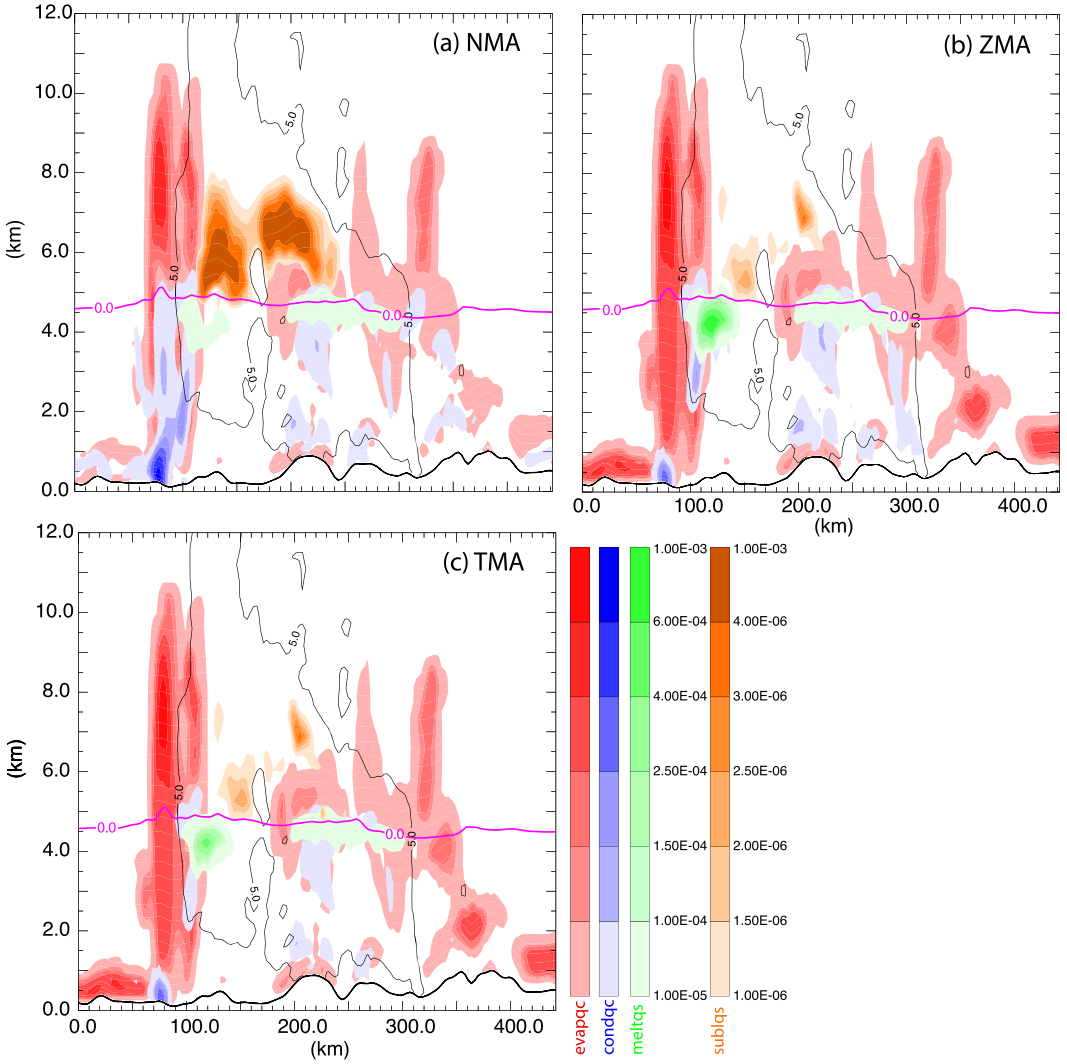

Figure 15. The cross sections of microphysical processes (red: cloud condensation; blue: cloud evaporation; green: snow melting; and orange: snow sublimation) from (a) NMA, (b) ZMA, and (c) TMA along A–B in Figure 3a at 2000 UTC, 23 April 2007. And the solid black line is 5 dBZ of mosaic reflectivity.

Figure 4 are plotted in Figures 14 and 15, respectively. It is worth noting that the average is done within the precipitation area where the reflectivity is greater than 5 dBZ. The increased water vapor in ZMA produces more cloud water below freezing levels (~5 km) for the stratiform regions, leading to more heating (Figures 14a and 15b) produced by cloud condensation than in TMA and NMA (Figures 15a and 15c). And those in TMA and NMA are comparable (Figures 14a, 15a, and 15c). The reduction of q_v ahead of the precipitation region (Figure 4) corresponds to greater cloud water evaporation rates in ZMA and TMA than in NMA (Figure 15), and the cooling produced by evaporation would suppress the spurious precipitation. Most of the cloud water evaporation in the precipitation area is above the freezing level (Figure 15), corresponding to the higher averaged cloud evaporation rates above the freezing level (Figure 14b). Near the freezing level, snow melting is the greatest in ZMA and the least in NMA. Above the freezing level, the q_v increments in ZMA and TMA are similar; snow sublimation is also similar in ZMA and TMA and is lower than that in NMA. It can be inferred that the latent heating below 6 km could be attributed mainly to cloud condensation, and the latent cooling above 6 km is caused mainly by snow sublimation (Figures 12 and 14).

5. Summary

In the cloud analysis system, properly updating moisture allows convection to be accurately maintained. Two MA schemes are investigated in our study. One adjusts *RH* according to cloud cover fraction proposed by Zhang (1999), the other one determines *RH* by using vertical velocity proposed by Tong (2015). Many studies have shown that Zhang scheme can lead to unrealistic warming in the middle troposphere, resulting in inaccurate forecasts. To improve the accuracy of analyses and forecasts, it has been suggested that the original humidity scheme be applied only to the first cycle in the intermittent rapid-refresh radar DA system. Tong scheme is tested with an idealized squall line case, resulted in significant improvement. Thus, it is necessary to investigate the impacts of two MA schemes on the analyses and subsequent forecasts.

A squall line that occurred in southeast China on 23–24 April 2007 is used to examine the aforementioned issues. Three sensitive experiments are conducted, including one without MA, one with the Zhang's MA scheme, and one with the Tong's MA scheme.

Both MA schemes reduce q_v in the region with spurious reflectivity in the background, especially in front of the convective line. Within the precipitation regions (reflectivity over 5 dBZ), both MA schemes generally increase q_v, while Zhang scheme adds more water vapor than Tong scheme. The major q_v differences between ZMA and TMA are below the freezing level within the precipitation region, due to the different MA procedures (Figure 2). By examining the subsequent forecasts after DA, results show that Tong scheme substantially improves the short-term forecasts in terms of both qualitative and quantitative verifications of the hourly precipitation, whereas Zhang scheme has no improvements compared to NMA. Tong scheme produces the best rainfall forecasts of the squall line in our test case, suggesting that it also produces the most reasonable moisture adjustment among the three experiments.

The latent heat release rates associated with 26 microphysical processes are diagnosed to investigate the microphysical responses to the MAs. Among all microphysical processes, cloud evaporation/condensation and snow sublimation/melting processes generally dominate the latent heating/cooling. Within precipitation region, the latent heating/cooling could be mainly attributed to cloud condensation/evaporation, whereas the latent cooling caused by snow sublimation above 6 km from NMA is comparable to cloud evaporation. The reductions of the water vapor mixing ratio within the spurious reflectivity regions, in front of the convective line in our case, increase the evaporation of cloud water, somehow suppress the false precipitation in the background. MAs increase moisture below the freezing level in the precipitation region, leading to less sublimation of snow, more condensation of cloud water and melting of snow. Owing to more water vapor being added by Zhang scheme, ZMA produces more heating than that in TMA through cloud condensation, likely induces the middle-low level overwarming.

In this study, results have shown that the humidity in initial condition has substantial impacts on the subsequent forecasts in terms of convective structure and rainfall prediction using a single squall line case. Analyzed RH according to vertical velocity helps suppress the spurious precipitation, improve stratiform precipitation prediction, and maintain the convective system in mesoscale DA system. However, the validation of RH-w relationships would require further examination, since the direct observations of *RH* and *w* are unavailable at the present. Also, the generality of the *RH-w* relationships would require further investigation with different convective system, such as supercell, front and so on, over different regions. Besides, microphysical schemes have potential impacts on the *RH-w* relationships, which also need to be investigated.

Acknowledgments
This work was supported primarily by the National Key R&D Program of China (grant 2017YFC1502104), the National Natural Science Foundation of China (grants 41775099, 41975123, and 41605026), and the Priority Academic Program Development of Jiangsu Higher Education Institutions. The NCEP Final Operational Global Analysis data can be freely obtained online (https://rda.ucar.edu/datasets/ds083.2). The ARPS model is provided by CAPS (http://www.caps.ou.edu/ARPS/arpsdown.html), and the radar data can be download online (http://data.cma.cn). The English in this document has been checked by at least two professional editors, both native speakers of English.

References

Albers, S. C., McGinley, J. A., Birkenheuer, D. L., & Smart, J. R. (1996). The local analysis and prediction system (LAPS): Analyses of clouds, precipitation, and temperature. *Weather and Forecasting*, *11*(3), 273–287. http://journals.ametsoc.org/doi/abs/10.1175/1520-0434%281996%29011%3C0273%3ATLAAPS%3E2.0.CO%3B2

Biggerstaff, M. I., & Houze, R. A. (1993). Kinematics and microphysics of the transition zone of the 10–11 June 1985 squall line. *Journal of the Atmospheric Sciences*, *50*(18), 3091–3110. http://journals.ametsoc.org/doi/abs/10.1175/1520-0469%281993%29050%3C3091%3AKAMOTT%3E2.0.CO%3B2

Broeke, M. S. V. D. (2017). Polarimetric radar metrics related to tornado life cycles and intensity in supercell storms. *Monthly Weather Review*, *145*(9), 3671–3686. https://journals.ametsoc.org/doi/abs/10.1175/MWR-D-16-0453.1

Chou, M.-D. (1990). Parameterizations for the absorption of solar radiation by O_2 and CO_2 with application to climate studies. *Journal of Climate*, *3*(2), 209–217. http://ssl123a48ffcc515f0d60df0827fb5ecc3471e.vpn.nuist.edu.cn/doi/abs/10.1175/1520-0442%281990%29003%3C0209%3APFTAOS%3E2.0.CO%3B2

French, M. M., Bluestein, H. B., Dowell, D. C., Wicker, L. J., Kramar, M. R., & Pazmany, A. L. (2008). High-resolution, mobile Doppler radar observations of cyclic mesocyclogenesis in a supercell. *Monthly Weather Review*, *136*(12), 4997–5016. https://journals.ametsoc.org/doi/abs/10.1175/2008MWR2407.1

Gao, J., & Stensrud, D. J. (2012). Assimilation of reflectivity data in convective-scale, cycled 3DVAR framework with hydrometeor classification. *Journal of the Atmospheric Sciences*, *69*, 1054–1065. https://doi.org/10.1175/JAS-D-11-0162.1

Gao, J., & Stensrud, D. J. (2014). Some observing system simulation experiments with a hybrid 3DEnVAR system for storm-scale radar data assimilation. *Monthly Weather Review*, *142*(9), 3326–3346. https://journals.ametsoc.org/doi/abs/10.1175/MWR-D-14-00025.1

Gao, J., Xue, M., Brewster, K., & Droegemeier, K. K. (2004). A three-dimensional variational data analysis method with recursive filter for Doppler radars. *Journal of Atmospheric and Oceanic Technology*, *21*(3), 457–469. http://journals.ametsoc.org/doi/abs/10.1175/1520-0426%282004%29021%3C0457%3AATVDAM%3E2.0.CO%3B2

Gao, J., Xue, M., Shapiro, A., & Droegemeier, K. K. (1999). A variational method for the analysis of three-dimensional wind fields from two Doppler radars. *Monthly Weather Review*, *127*(9), 2128–2142. http://journals.ametsoc.org/doi/abs/10.1175/1520-0493%281999%29127%3C2128%3AAVMFTA%3E2.0.CO%3B2

Grabowski, W. W., & Morrison, H. (2017). Modeling condensation in deep convection. *Journal of the Atmospheric Sciences*, *74*(7), 2247–2267. https://journals.ametsoc.org/doi/abs/10.1175/JAS-D-16-0255.1

Grabowski, W. W., Morrison, H., Shima, S.-I., Abade, G. C., Dziekan, P., & Pawlowska, H. (2019). Modeling of cloud microphysics: Can we do better? *Bulletin of the American Meteorological Society*, *100*(4), 655–672. https://journals.ametsoc.org/doi/abs/10.1175/BAMS-D-18-0005.1

Houtekamer, P. L., & Zhang, F. (2016). Review of the ensemble Kalman filter for atmospheric data assimilation. *Monthly Weather Review*, *144*(12), 4489–4532. https://doi.org/10.1175/MWR-D-15-0440.1

Hu, M., & Xue, M. (2007). Impact of configurations of rapid intermittent assimilation of WSR-88D radar data for the 8 May 2003 Oklahoma City tornadic thunderstorm case. *Monthly Weather Review*, *135*(2), 507–525. https://doi.org/10.1175/MWR3313.1

Hu, M., Xue, M., & Brewster, K. (2006). 3DVAR and cloud analysis with WSR-88D Level-II data for the prediction of the Fort Worth, Texas, tornadic thunderstorms. Part I: Cloud analysis and its impact. *Monthly Weather Review*, *134*(2), 675–698. https://doi.org/10.1175/MWR3092.1

Hu, M., Xue, M., Gao, J., & Brewster, K. (2006). 3DVAR and cloud analysis with WSR-88D level-II data for the prediction of the Fort Worth, Texas, tornadic thunderstorms. Part II: Impact of radial velocity analysis via 3DVAR. *Monthly Weather Review*, *134*(2), 699–721. https://doi.org/10.1175/MWR3093.1

Jung, Y., Xue, M., & Tong, M. (2012). Ensemble Kalman filter analyses of the 29–30 May 2004 Oklahoma tornadic thunderstorm using one- and two-moment bulk microphysics schemes, with verification against polarimetric radar data. *Monthly Weather Review*, *140*(5), 1457–1475. http://journals.ametsoc.org/doi/abs/10.1175/MWR-D-11-00032.1

Jung, Y., Zhang, G., & Xue, M. (2008). Assimilation of simulated polarimetric radar data for a convective storm using the ensemble Kalman filter. Part I: Observation operators for reflectivity and polarimetric variables. *Monthly Weather Review*, *136*(6), 2228–2245. https://doi.org/10.1175/2007MWR2083.1

Kain, J. S., Xue, M., Coniglio, M. C., Weiss, S. J., Kong, F., Jensen, T. L., et al. (2010). Assessing advances in the assimilation of radar data within a collaborative forecasting-research environment. *Weather and Forecasting*, *25*, 1510–1521. http://doi.org/10.1175/2010WAF2222405.1

Kennedy, P. C., Westcott, N. E., & Scott, R. W. (1993). Single-Doppler radar observations of a mini-supercell tornadic thunderstorm. *Monthly Weather Review*, *121*(6), 1860–1870. https://journals.ametsoc.org/doi/abs/10.1175/1520-0493%281993%29121%3C1860%3ASDROOA%3E2.0.CO%3B2

Kong, R., Xue, M., & Liu, C. (2018). Development of a hybrid En3DVar data assimilation system and comparisons with 3DVar and EnKF for radar data assimilation with observing system simulation experiments. *Monthly Weather Review*, *146*(1), 175–198. https://journals.ametsoc.org/doi/abs/10.1175/MWR-D-17-0164.1

Li, Y., Wang, X., & Xue, M. (2012). Assimilation of radar radial velocity data with the WRF hybrid Ensemble-3DVAR system for the prediction of hurricane Ike (2008). *Monthly Weather Review*, *140*(11), 3507–3524. https://journals.ametsoc.org/doi/abs/10.1175/MWR-D-12-00043.1

Liu, C., Xue, M., & Kong, R. (2019). Direct assimilation of radar reflectivity data using 3DVAR: Treatment of hydrometeor background errors and OSSE tests. *Monthly Weather Review*, *147*(1), 17–29. https://journals.ametsoc.org/doi/abs/10.1175/MWR-D-18-0033.1

Liu, C., Xue, M., & Kong, R. (2020). Direct variational assimilation of radar reflectivity and radial velocity data: Issues with nonlinear reflectivity operator and solutions. *Monthly Weather Review*. https://doi.org/10.1175/MWR-D-19-0149.1

Lynch, P., & Huang, X.-Y. (1992). Initialization of the HIRLAM model using a digital filter. *Monthly Weather Review*, *120*(6), 1019–1034. http://journals.ametsoc.org/doi/abs/10.1175/1520-0493%281992%29120%3C1019%3AIOTHMU%3E2.0.CO%3B2

Milbrandt, J. A., & Yau, M. K. (2005). A multimoment bulk microphysics parameterization. Part I: Analysis of the role of the spectral shape parameter. *Journal of the Atmospheric Sciences*, *62*(9), 3051–3064. https://doi.org/10.1175/JAS3534.1

Noilhan, J., & Planton, S. (1989). A simple parameterization of land surface processes for meteorological models. *Monthly Weather Review*, *117*(3), 536–549. http://ssl123a48ffcc515f0d60df0827fb5ecc3471e.vpn.nuist.edu.cn/doi/abs/10.1175/1520-0493%281989%29117%3C0536%3AASPOLS%3E2.0.CO%3B2

Pan, Y., & Wang, M. (2019). Impact of the assimilation frequency of radar data with the ARPS 3DVar and cloud analysis system on forecasts of a squall line in southern China. *Advances in Atmospheric Sciences*, *36*(2), 160–172. https://doi.org/10.1007/s00376-018-8087-5

Pan, Y., Xue, M., & Ge, G. (2016). Incorporating diagnosed intercept parameters and the graupel category within the ARPS cloud analysis system for the initialization of double-moment microphysics: testing with a squall line over south China. *Monthly Weather Review*, *144*(1), 371–392. https://doi.org/10.1175/MWR-D-15-0008.1

Schaefer, J. T. (1990). The critical success index as an indicator of warning skill. *Weather and Forecasting*, *5*(4), 570–575. https://journals.ametsoc.org/doi/abs/10.1175/1520-0434%281990%29005%3C0570%3ATCSIAA%3E2.0.CO%3B2

Schenkman, A. D., Xue, M., Shapiro, A., Brewster, K., & Gao, J. (2011). The analysis and prediction of the 8–9 May 2007 Oklahoma tornadic mesoscale convective system by assimilating WSR-88D and CASA radar data using 3DVAR. *Monthly Weather Review*, *139*(1), 224–246. http://journals.ametsoc.org/doi/abs/10.1175/2010MWR3336.1

Smull, B. F., & Houze, R. A. Jr. (1987). Dual-Doppler radar analysis of a midlatitude squall line with a trailing region of stratiform rain. *Journal of the Atmospheric Sciences*, *44*(15), 2128–2149. https://journals.ametsoc.org/doi/abs/10.1175/1520-0469%281987%29044%3C2128%3ADDRAOA%3E2.0.CO%3B2

Sun, J., & Crook, N. A. (1997). Dynamical and microphysical retrieval from doppler radar observations using a cloud model and its adjoint. Part I: Model development and simulated data experiments. *Journal of the Atmospheric Sciences*, *54*(12), 1642–1661. http://journals.ametsoc.org/doi/abs/10.1175/1520-0469%281997%29054%3C1642%3ADAMRFD%3E2.0.CO%3B2

Sun, W.-Y., & Chang, C.-Z. (1986). Diffusion model for a convective layer. Part I: Numerical simulation of convective boundary layer. *Journal of Climate and Applied Meteorology*, *25*, 1445-1453. https://doi.org/10.1175/1520-0450(1986)025<1445:DMFACL>2.0.CO;2

Takemi, T. (2006). Impacts of moisture profile on the evolution and organization of midlatitude squall lines under various shear conditions. *Atmospheric Research*, *82*(1), 37–54. http://www.sciencedirect.com/science/article/pii/S0169809506000251

Takemi, T. (2007). A sensitivity of squall-line intensity to environmental static stability under various shear and moisture conditions. *Atmospheric Research*, *84*(4), 374–389. http://www.sciencedirect.com/science/article/pii/S0169809506002353

Tong, C. (2015). Limitations and potential of complex cloud analysis and its improvement for radar reflectivity data assimilation using OSSEs. (Ph.D. Dissertation), University of Oklahoma.

Tong, M. J., & Xue, M. (2005). Ensemble Kalman filter assimilation of doppler radar data with a compressible nonhydrostatic model: OSS experiments. *Monthly Weather Review*, *133*(7), 1789–1807. https://doi.org/10.1175/MWR2898.1

Wang, H. L., Sun, J. Z., Fan, S. Y., & Huang, X. Y. (2013). Indirect assimilation of radar reflectivity with WRF 3D-Var and its impact on prediction of four summertime convective events. *Journal of Applied Meteorology and Climatology*, *52*, 889–902.

Wang, H. L., Sun, J. Z., Zhang, X., Huang, X. Y., & Auligne, T. (2013). Radar data assimilation with WRF 4D-Var. Part I: System development and preliminary testing. *Monthly Weather Review*, *141*, 2224–2244.

Xu, Q., Gao, J., & Gu, W. (1998). Generalized adjoint for physical processes with parameterized discontinuities. Part V: Coarse-grain adjoint and problems in gradient check. *Journal of the Atmospheric Sciences*, *55*(11), 2130–2135. https://journals.ametsoc.org/doi/abs/10.1175/1520-0469%281998%29055%3C2130%3AGAFPPW%3E2.0.CO%3B2

Xue, M., Droegemeier, K. K., & Wong, V. (2000). The advanced regional prediction system (ARPS)—A multi-scale nonhydrostatic atmospheric simulation and prediction model. Part I: Model dynamics and verification. *Meteorology and Atmospheric Physics*, *75*(3), 161–193. https://doi.org/10.1007/s007030070003

Xue, M., Droegemeier, K. K., Wong, V., Shapiro, A., Brewster, K., Carr, F., et al. (2001). The advanced regional prediction system (ARPS)—A multi-scale nonhydrostatic atmospheric simulation and prediction tool. Part II: Model physics and applications. *Meteorology and Atmospheric Physics*, *76*(1-4), 143–165. https://doi.org/10.1007/s007030170027

Xue, M., Tong, M., & Droegemeier, K. K. (2006). An OSSE framework based on the ensemble square root Kalman filter for evaluating the impact of data from radar networks on thunderstorm analysis and forecasting. *Journal of Atmospheric and Oceanic Technology*, *23*(1), 46–66. https://doi.org/10.1175/JTECH1835.1

Zhang, J. (1999). Moisture and diabatic initialization based on radar and satellite observations. (Ph.D. Dissertation), University of Oklahoma.

Zhao, K., & Xue, M. (2009). Assimilation of coastal Doppler radar data with the ARPS 3DVAR and cloud analysis for the prediction of Hurricane Ike (2008). *Geophysical Research Letters*, *36*, L12803. https://doi.org/10.1029/2009GL038658